Supporting Information

Seto et al. 10.1073/pnas.1109243109

SI Text

SI Materials and Methods. ***Elemental analysis.*** Ca^{2+} and Mg^{2+} concentrations were determined using optical emission spectroscopy (λ_{Mg}: 285.213 nm, λ_{Ca}: 317.933 nm) with inductively coupled plasma (ICP) using an Optima 3000 (Perkin Elmer). 15 mg of ground sea urchin spine were dissolved in 2 ml of 30% HCl and 2 ml of 65% HNO_3 in a "Multiwave" microwave disintegration device (Anton Paar). Two samples were disintegrated and each of them was diluted with 100 mL distilled water. The instrument was calibrated with standards Mg = 1 & 10 ppm and Ca = 1, 10, 100 ppm.

SEM. The adult sea urchin spines were fractured using tweezers. A few fractured sea urchin spines were etched in water overnight at room temperature. The freshly prepared fracture surfaces and the etched fracture surfaces of the spines were characterized by SEM (LEO 1550-GEMINI, LEO Electron Microscopy Group). Thin sections of thickness 1,000 nm were prepared using microtomy.

TGA. Thermogravimetry analysis measurements were performed with a Netzsch STA 429 (Netzsch GmbH) in the presence of a nitrogen atmosphere. Approximately 49 mg of the ground sea urchin spine were weighed and used for the measurements. The sample was heated at a rate of 5 °C/ min until a final temperature of 1,000 °C.

TEM. Sea urchin spines were embedded in Spurr's resin (TEM) and LR-white (HRTEM) by vacuum infiltration. For TEM analysis sections were cut to a thickness of 50–100 nm with an RMC ultramicrotome using a diamond knife. Sections were floated onto either water or ethylene glycol and collected onto 3 mm copper mesh grids. TEM/HRTEM analyses were performed using a JEOL JEM 1200 EX (JEOL GmbH) and a JEOL JEM-2100F-UHR (JEOL GmbH), respectively.

WAXS/SAXS/USAXS. All (U)SAXS experiments were performed on samples embedded in PMMA and cut in a transverse direction with respect to the main spicule axis using a precision low-speed circular saw (Accutome 5, Struers Tech A/S, Copenhagen, Denmark). The outer diameter of the spicule section was in the order of 1.4 mm. The 500 μm thick samples were further reduced to approximately 100 μm by careful polishing with high grade paper (SiC 2400) in order to avoid the presence of microcracks which were found to be problematic for (U)SAXS analysis. The accessible q-range was 0.001–0.3 nm^{-1} corresponding to 20–6300 nm in real space.

WAXS was performed on a Bruker D8 Advance (Bruker AXS Gmbh) using a Göbel mirror and parallel beam geometry at 40 kV 40 mA.

The laboratory SAXS machine provided a monochromatic beam of wavelength $\lambda_{CuK\alpha} = 0.154$ nm (8.041 keV) was reduced to approximately 100 μm in diameter at sample position using a combination of three apertures. Several frames were collected in steps of 100 μm across the sample to test possible differences from the core to the outer part of the spicule. This enabled a q-space resolution of 0.13–2 nm^{-1} to be obtained. This corresponds to features in the order of 3–50 nm in real space.

SAXS analysis. Radial profile of the scattered intensity (arbitrary units) was measured using a low resolution laboratory instrument. Two regions, indicated on the graph, follow a law of the type $I = P/q^4$ (or, $\log I = \log P - 4 \times \log q$) where P is a constant, which is typical for a dense two-phased system with sharp boundaries. A linear fit of the logarithmic plot was performed within the boundaries indicated by the dotted lines. The result of the fit is shown by the dashed lines; the slopes in the $\log I$ vs $\log q$ plot were 4.01 and −3.98 for region 1 and 2 respectively. Similarly, a slope of −2.06 was obtained in the intermediate region. In the schematic, region 1 is the calcite nanoparticle (blue), whereas region 2 represents occluded areas within the nanoparticle (pink).

At the ESRF beamline, an X-ray beam monochromatized to a wavelength of $\lambda = 0.0995$ nm (12.460 keV) was collimated to approximately 200 μm in diameter. Two separate measurements using both a pinhole camera and a Bonse-Hart setup were combined for very high angular resolution, thus spanning a large part of the ultrasmall angle X-ray scattering (USAXS) regime.

X-ray single crystal structure determination. The vertex of a sea urchin spine was mounted on a glass fiber. Intensity data were collected at room temperature using a STOE Imaging Plate Diffraction System IPDS-2 with graphite monochromatized MoKα radiation ($\lambda = 0.71073$ Å) at 50 kV and 40 mA (180 frames, $\Delta\omega = 1°$, 1 min exposure time per frame). The data were corrected by a spherical absorption correction using the program X-Area (Stoe, 2004) as well as for Lorentz, polarization and extinction effects. The structure was solved with SHELXS-97 using direct methods and refined with SHELXL-97 (S1). All atoms were refined anisotropically. At the beginning, the refinement was performed only with calcium as the cation. After convergence of the refinement, magnesium was introduced on the cation sites. The sum of the site occupation factors (sofs) of Ca and Mg was constrained to equal the full occupancy of the cation site. Finally, the Ca and Mg site occupation factors were refined free to give a sof ratio of 0.96 to 0.04 (Ca to Mg). The unit cell parameters were estimated with 3,182 reflections. Further details of the crystal structure investigation may be obtained from Fachinformationszentrum Karlsruhe, 76344 Eggenstein-Leopoldshafen, Germany [(fax: (+49)7247-808-666; e-mail: crysdata@fiz-karlsruhe.de, http://www.fiz-karlsruhe.de/request_for_deposited_data.html]on quoting the deposition number CSD-419785.

SAXS/WAXS analysis. The 2D SAXS patterns were corrected for detector artifacts, normalized and azimuthally averaged using the FIT2D software package (S2) for the SAXS dataset and a software package developed at the ID02 beamline (S3) for the USAXS measurements. The 1D radial profiles were then analyzed using additional software, written in Python language, developed by one of the authors (A. Gourrier) for SAXS/WAXS analysis.

While the sharp peaks measured with WAXS only yield dimensions from the coherently scattering parts of a sample, SAXS provides coherence lengths of volumes where the average electron density differs from the bulk, independently of the relative degree of ordering. The intensity of the SAXS signal therefore directly depends on the difference in the electron density between the two phases. In order to check for the possibility of measuring a signal originating from the ACC fraction in the calcite surrounding, the scattering contrast was calculated. A value of $\Delta\rho \sim 9.2.10^{10}$ cm^{-2} was found, based on mass densities of 2.71 g/mL for calcite and 1.62 g/mL for ACC (S4) (neglecting Mg^{2+} and water in the ACC), which is sufficient to observe the ACC phase.

The analysis of the region of the radial profile at high q (region 2 in Fig. 3) was performed by subtracting the contribution at low q using a law of the form: $I = P_1/q^4$. The resulting curve is shown in Fig. S9 (*Top left*). This allowed calculating a correlation length according to a procedure described previously (36) and defined by: $T = 4J/\pi P$ where $P = \lim_{q\to\infty}(q^4 I(q))$ and $J = \int_0^\infty q^2 I(q) dq$ (S5).

Nano-X-ray diffraction (nano-XRD). A transverse section of approximately 50 μm was prepared using the protocol described in the SAXS measurements section of the SI. This section was mounted on a translation stage which is, itself, fixed to a rotation stage at beamline ID13 (ESRF). The 2D data were collected using a Frelon detector of $2K \times 2K$ pixels with size of 50×50 μm^2 and processed with the softwares Fit2D and PySXIm (custom designed Python software) after removal of the parasitic scattering.

A X-ray beam at beamline ID13 (ESRF) was monochromatized to an energy of 15.26(5) keV ($\lambda = 0.812(2)$ Å) and focused in two steps using Be lenses and parabolic X-ray refractive lenses to a focal spot size of 70 nm at FWHM (S6). Sample regions were identified using an online optical microscope and the sample-to-detector distance was calibrated using AgBh (S7).

Due to the single-crystalline nature of the sample, two different measurements were undertaken:

Measurement type 1: Estimation of the degree of rotational disorder in a localized volume: Rough rotational scans were acquired about the radial direction of the sample (ω) within ±5° with 0.1° steps in order to locate a diffraction spot of interest in reciprocal space (Fig. S9*C*). The sum of the 2D patterns within this rotational range is shown in Fig. 2*A*. The sample was then positioned to the position ω_{MAX} of maximum peak intensity (Fig. S9*C*, *Left*) and scanned within ±1° with finner steps of 0.02°. The intensity peak profile was calculated by integrating the intensity within a narrow region of interest around the peak (30×30 pixels). The FWHM in the ω direction was calculated to be 0.10° (Fig. S9*C*, *Top right*). At the maximum intensity position, the azimuthal profile was calculated (Fig. S9*C*, *Bottom right*) within the cake region indicated in Fig. S9*C*, *Center*. The FWHM was calculated to be 0.73°. Due to the sample thickness, it is assumed that the number of nanocrystals in the volume probe by the beam is in the order of 500 when the beam is normal to the sample section. In order enhance the accuracy of the measurement, this measurement was repeated with a beam translated laterally by steps of 5 μm over a distance of 60 μm. The results remain essentially unchanged. Both measures are thus sufficient to fully characterize the 3D extent of the peak.

Measurement type 2: In order to obtain a more statistical view of the regularity in crystalline orientation, a line scan was recorded along the radial direction of the spicule section, from the centre to the outermost part, indicated by the red dots in Fig. S9*B*. This scan was performed at the ω_{MAX} peak intensity value. The results are summarized in Fig. S9*D*. It can be observed that the peak position varies within a range of $\Delta\chi = 0.18°$ (99% of the data) only over a distance of 600 μm. Similarly, the FWHM varies by $\Delta\chi = 0.2°$ (99% of the data).

μ-Computer tomography (μ-CT). A single adult Authoeidaris Erassispina sea urchin spine was oriented with UV-cured dental epoxy such that its longitudinal axis was perpendicular to the incoming X-ray beam. A Skyscan 1072 μ-CT table-top scanner (Skyscan) was used to scan the dry sample for approximately 5 h (with integration times of 4 s and obtaining 824 images using a cone-beam geometry). Following reconstruction, volume rendering and visualization of the 3D microstructure were performed with Amira 4.0 (Mercury Computer Systems).

Atomic force microscopy. Representative adult sea urchin and calcined were embedded in PMMA [poly(methyl methcrylate)]. Each sample was sectioned with a 300 μm diamond blade using a low-speed saw (Isomet Low Speed Saw, Buehler Ltd.) perpendicular to the longitudinal plane of tranverse plane. The sectioned surfaces of each sample were polished with 3 μm and 1 μm diamond particles (DP-Spray P, Struers A/S, Ballerup), respectively, with an automatic polisher (Logitech PM5, Logitech Ltd.) until the average surface roughness was approximately 1 μm. Surface topology imaging with an atomic force microscopy (Dimension 3100, Veeco Instruments) along the diameter of each spine was performed on the polished surfaces.

Focused ion beam. Powdered samples were placed onto 400 mesh copper TEM grids (Quantifoil Micro Tools GmbH) coated with carbon. The TEM grids with samples were placed onto a custom TEM grid sample holder and placed into a FESEM (Zeiss CrossBeam 1540XB, Zeiss SMT GmbH) equipped with a Ga^+ ion 30 kV FIB column. Areas of 60×60 μm regions (area between mesh) were exposed to Ga^+ ion exposure at specific doses. After FIB treatment, the sample grids were examined under a TEM.

Details of the NMR analysis. Repetition times of 60 s, 300 s, 600 s, 3,600 s and 7,200 s were used for the direct excitation using a ^{13}C 90° pulse length of 6 μs.

For the $^1H\{^{13}C\}$ cross-polarization (CP) measurements, 12 k transients were acquired with CP times of 1 ms and 8 ms using TPPM decoupling. The ^1H 90° pulse length was 4 μs and repetition times of 2 s were used. The ^1H spin lock pulse was ramped down to 50% during CP to broaden the CP match condition. The ^{13}C chemical shifts were referenced using adamantane (CH signal set to 38.5 ppm relative to TMS) as a secondary standard.

Fig. S13*A* shows two NMR spectra acquired with single pulse excitation (SP) and at different repetition times of 1 min and 120 min (spectra in the middle and at the bottom). Both spectra are plotted and normalized to show that the line shape changes considerably with increasing repetition time. The ^{13}C NMR line is broad for the "short" repetition time of 1 min, whereas a narrow component appears in addition for the spectrum acquired with 120 min relaxation delay (*Bottom*). Obviously, the spectrum must consist of two differently relaxing components. In fact, two time constants are obtained for the ^{13}C spin-lattice relaxation behavior (not shown here): (*i*) one time constant with about 102 min for the narrow line at 168.55 ppm, and a second time constant of about 5 min for the broader line. In addition, $^1H\{^{13}C\}$ cross-polarization (CP) is effective in this sample. The 1 ms CP spectrum is shown as a top trace in Fig. S13*A*). This CP line is slightly downfield shifted in comparison with the two other components and it has about a 30% larger line width compared with the broader of the other two lines (cf. Table 1). More importantly, the CP effect is very low such that out of all ^{13}C in the sample, only a minor part is contained in that structure for which we assume is ACC.

The line widths and positions of the fast relaxing broad and extraordinarily long relaxing narrow components were obtained by subtracting the two spectra (1 min and 120 min repetition times) from each other with proper scaling factors such that either the narrow or the broad component remain. The result of the procedure is shown schematically in Fig. S13*B* for the ^{13}C NMR spectrum with 120 min repetition time. These two different line shapes show the narrow and broader components separated, and these two spectra were then fitted separately using a single Gaussian for each of these lines to get reliable parameters for widths and positions. This difference procedure was chosen because a simple fit does not yield unique values for positions and width as the lines overlap strongly. Finally, the ^{13}C MAS NMR spectrum was fitted using fixed line positions and widths for these two lines and a third, broader component to take into account the CP spectrum. The relative peak areas for the three

lines are listed in Table 1; the numbers in the last column give the relative amounts of carbons in these three lines. However, a T_1 intensity correction factor is required for the narrow line at 168.55 ppm because two ^{13}C MAS NMR spectra with relaxation delays of 60 min and 120 min were added to increase the signal-to-noise ratio (equal number of scans in each experiment). These delays are on the order of the T_1 time of the narrow signal (102 min). Hence, the T_1 intensity correction factor amounts to 1.84 (for the narrow line only) and is the average of $1.44 = 1/(1 - \exp(-120/102))$ and $2.24 = 1/(1 - \exp(-60/102))$; T_1 relaxation time: 102 min, repetition times in experiments: 120 min and 60 min, respectively.

1. Sheldrick GM, Schneider TR (1997) SHELXL: High resolution refinement. *Method Enzymol* 277:319–343.
2. Hammersley AP (1997) *ESRF Internal Report*. Report No. ESRF97, HA02T; European Synchrotron Radiation Facility: Grenoble Cedex, France.
3. Boesecke, P (2007) Reduction of two-dimensional small- and wide angle X-ray scattering data *J. Appl Cryst* 40:s423–s427.
4. Bolze J, et al. (2002) Formation and Growth of Amorphous Colloidal CaCO3 Precursor Particles as detected by Time-resolved SAXS. *Langmuir* 18:8364–8369.
5. Porod G (1952) Die Röntgenkleinwinkelstreuung von dichtgepackten kolloiden Systemen. II. Teil. *Kolloid Z.* 125:51–57.
6. Schroer, et al. (2005) 'Hard x-ray nanoprobe based on refractive x-ray lenses. *Appl Phys Lett* 87:124103–124106.
7. Blanton, et al. (1995) JCPDS—International Centre for Diffraction Data round robin study of silver behenate. A possible low-angle X-ray diffraction calibration standard. *Powder Diffr* 10:91–95.
8. Li X, Xu ZH, Wang R In situ observation of nanograin rotation and deformation in nacre. (2006) *Nano Lett* 6:2301.
9. Glatter O, Kratky O (1982) *Small-Angle X-ray Scattering* (New York, Academic).

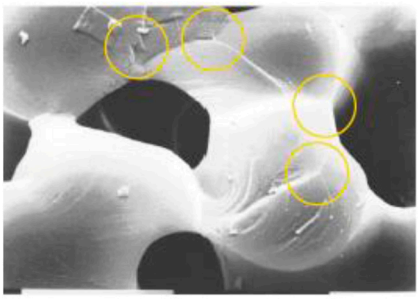

(S. Weiner, Addadi, L., *Journal of Materials Chemistry* **7**, 689 (1997)., scale bar=10 μm)

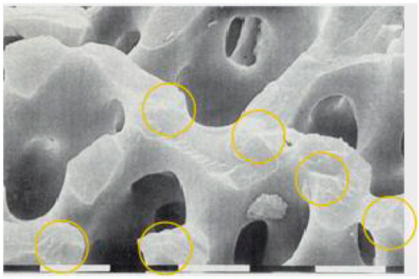

(H. A. Lowenstam, Weiner, S., *On Biomineralization* (Oxford University Press, New York, 1989), pp. 323., scale bar=10 μm)

Fig. S1. SEM images of the fracture surface of sea urchin spine from other authors in the literature. The yellow circles highlight crystalline-like facets among the chonchoidal fracture surfaces.Top image from: Weiner S, Addadi L (1997) *J. Mater. Chem.*, 7, 689-702. http://dx.doi.org/10.1039/A604512J. Reproduced by permission of The Royal Society of Chemistry. Scale bar=10 μm. Bottom image from: Lowenstam HA, Weiner S (1989) *On Biomineralization,* by permission of Oxford University Press, Inc, www.oup.com. Scale bar=10 μm.

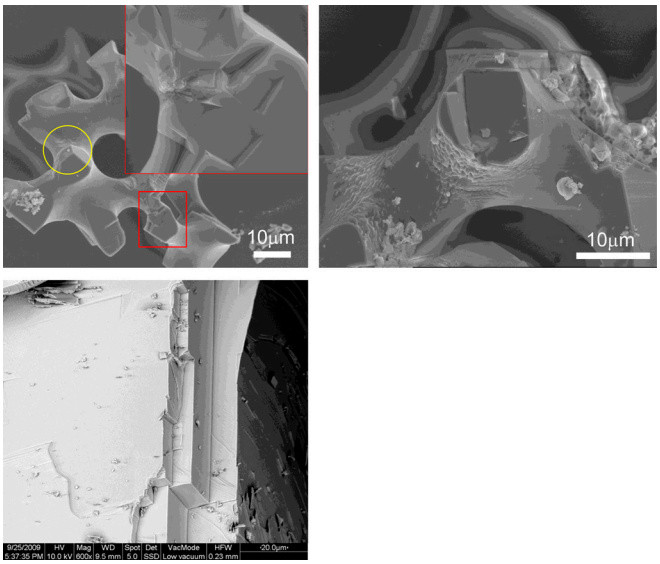

Fig. S2. Cleavage planes of a single crystal sea urchin spine replica (*Upper*) and a cleavage plane of geological calcite (*Lower*). The flat {104} cleavage planes are clearly visible. The yellow circle shows the similar {104} fracture to those observed in Fig. 1*A* (circles) and Fig. S1.

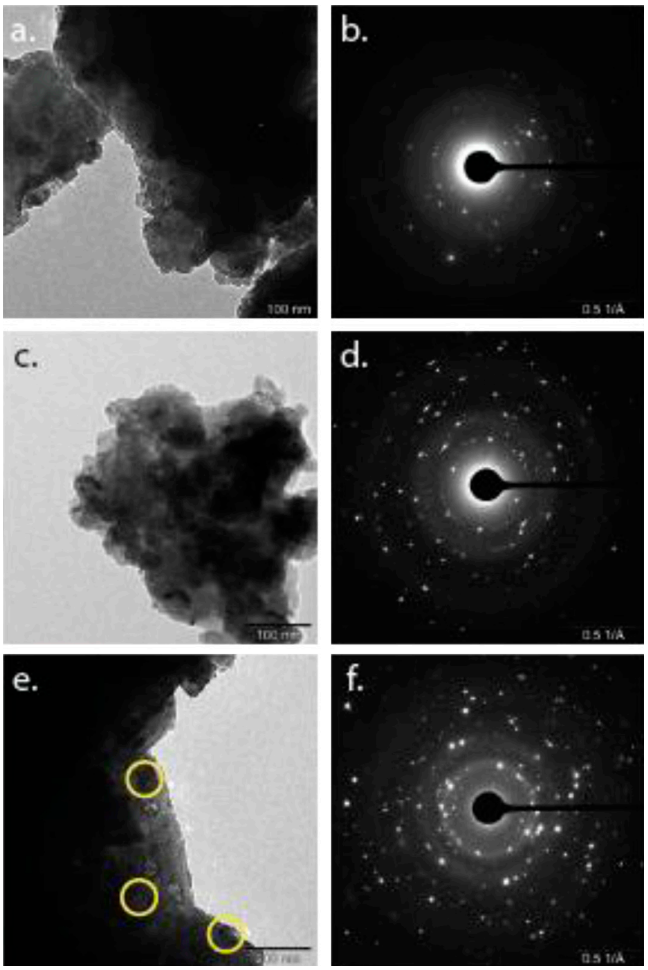

Fig. S3. FIB effects on the microstructure of sea urchin spine samples (*A*) TEMmicrograph of a powdered sample from a sea urchin spine without FIB [scale bar = 100 nm] (*B*) Electron diffraction pattern of (*A*) (*C*) TEM micrograph of a powdered sample from a sea urchin spine with FIB exposure at 50 $\mu A \times$ sec $/cm^2$ [scale bar = 100 nm] (*D*) Electron diffraction pattern of (*C*) (*E*) TEM micrograph of a powdered sample from a sea urchin spine with FIB exposure at 500 $\mu A \times$ sec $/cm^2$ [scale bar = 200 nm] with areas of microstructural beam damage highlighted in yellow (*F*) Electron diffraction pattern of (*E*).

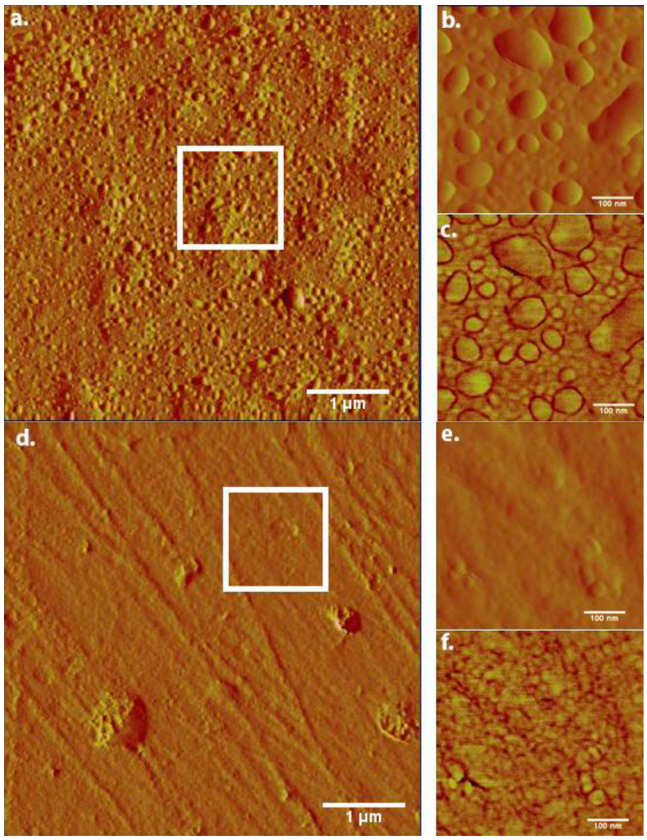

Fig. S4. AFM amplitude and phase images of a polished native and calcined ($T = 450$ °C) sea urchin spine transverse plane at different magnifications (*A*)–(*B*.) Granular structures can be observed in the amplitude images of the native spine at various magnifications similar to observations by Wang and coworkers in nacre (S8) (*C*) The corresponding phase image of (*B*.) highlighting the different mechanical stiffness of the granular structures (*D*)–(*E*.) Calcination processes alter the granular structures in the spine, seemingly making the material more homogenous (*F*) The phase image of (*E*) showing the homogeneity of the microstructure.

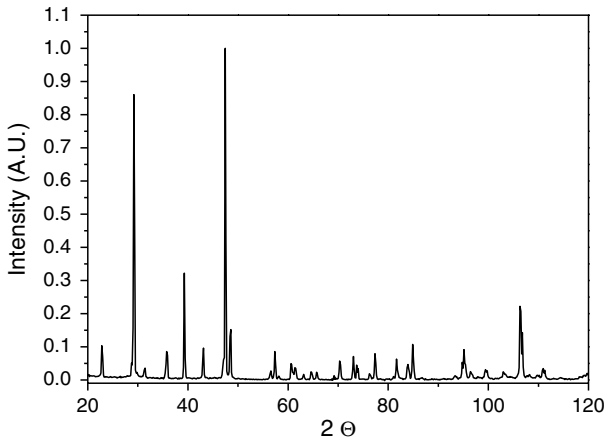

Fig. S5. Wide angle XRD diffractogram of a powdered sea urchin spine.

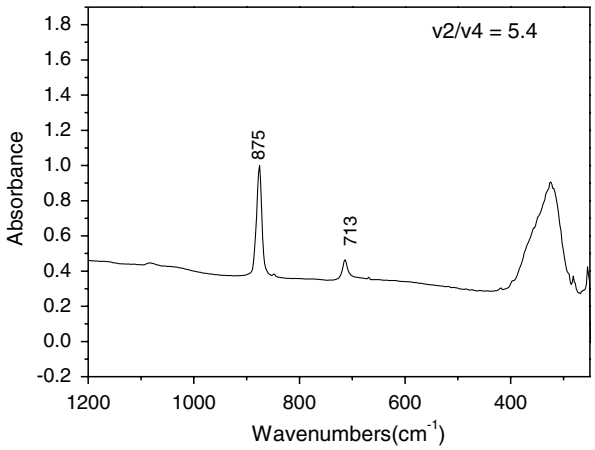

Fig. S6. FTIR of a powdered sea urchin spine

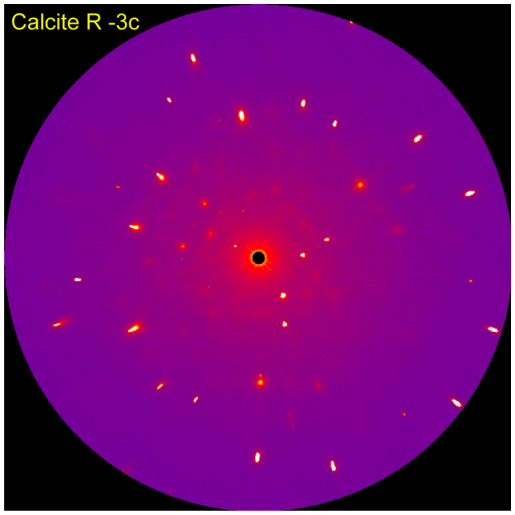

Fig. S7. Image from single crystal analysis of a sea urchin spine.

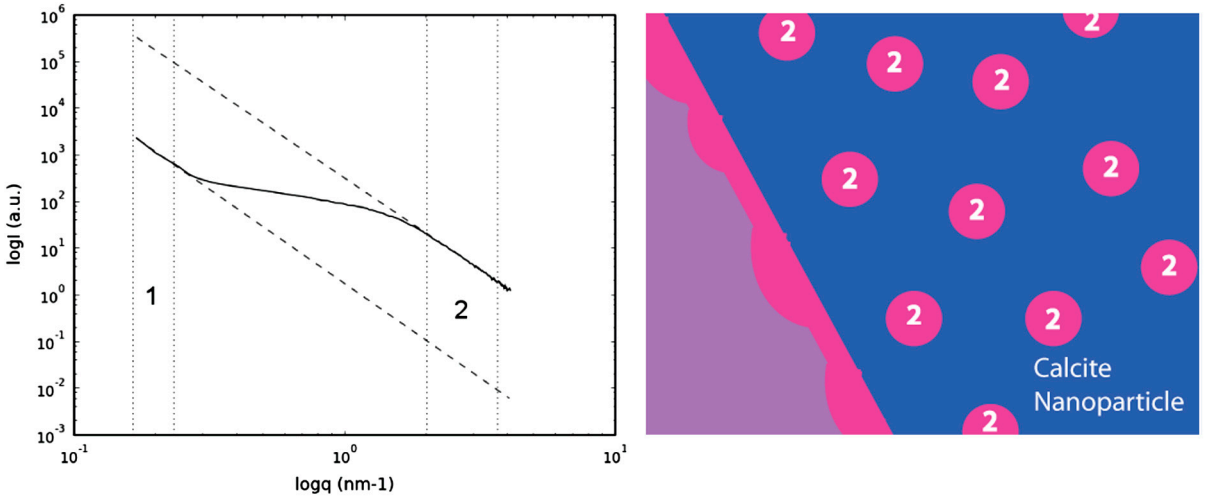

Fig. S8. Radial profile of the scattered intensity (arbitrary units) measured using a low resolution laboratory instrument. Two regions, indicated on the graph, follow a law of the type $I = P/q^4$ (or, $\log I = \log P - 4 \times \log q$) where P is a constant, which is typical for a dense two-phased system with sharp boundaries. In the schematic, region 1 is the calcite nanoparticle (blue), whereas region 2 represents occluded areas within the nanoparticle (pink).

A

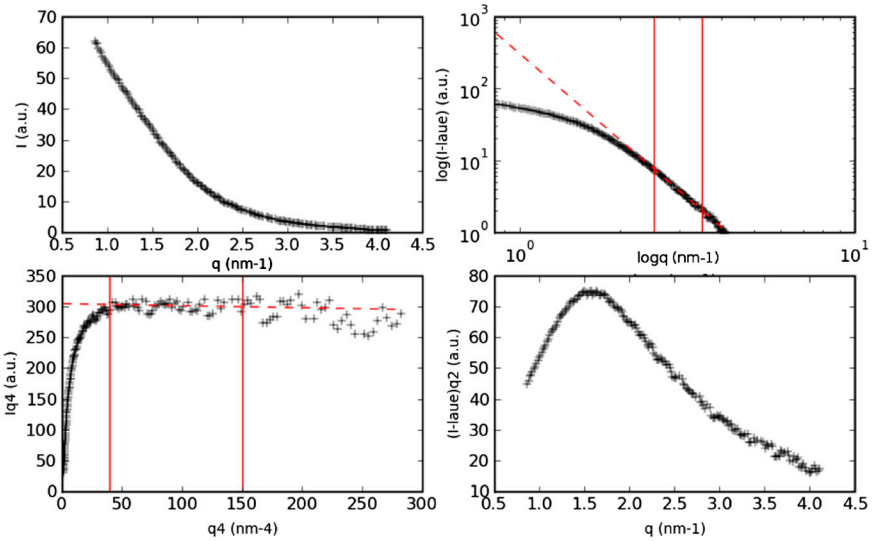

$w = 1/[\sigma^2(F_o^2)+(0.0219P)^2+0.1271P]$ where $P=(F_o^2+2F_c^2)/3$

B

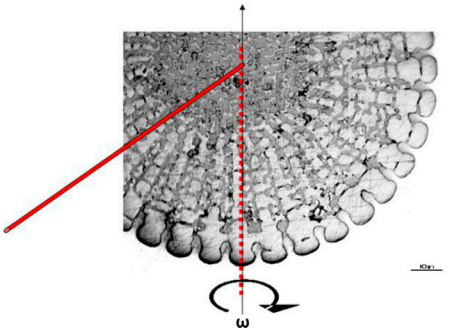

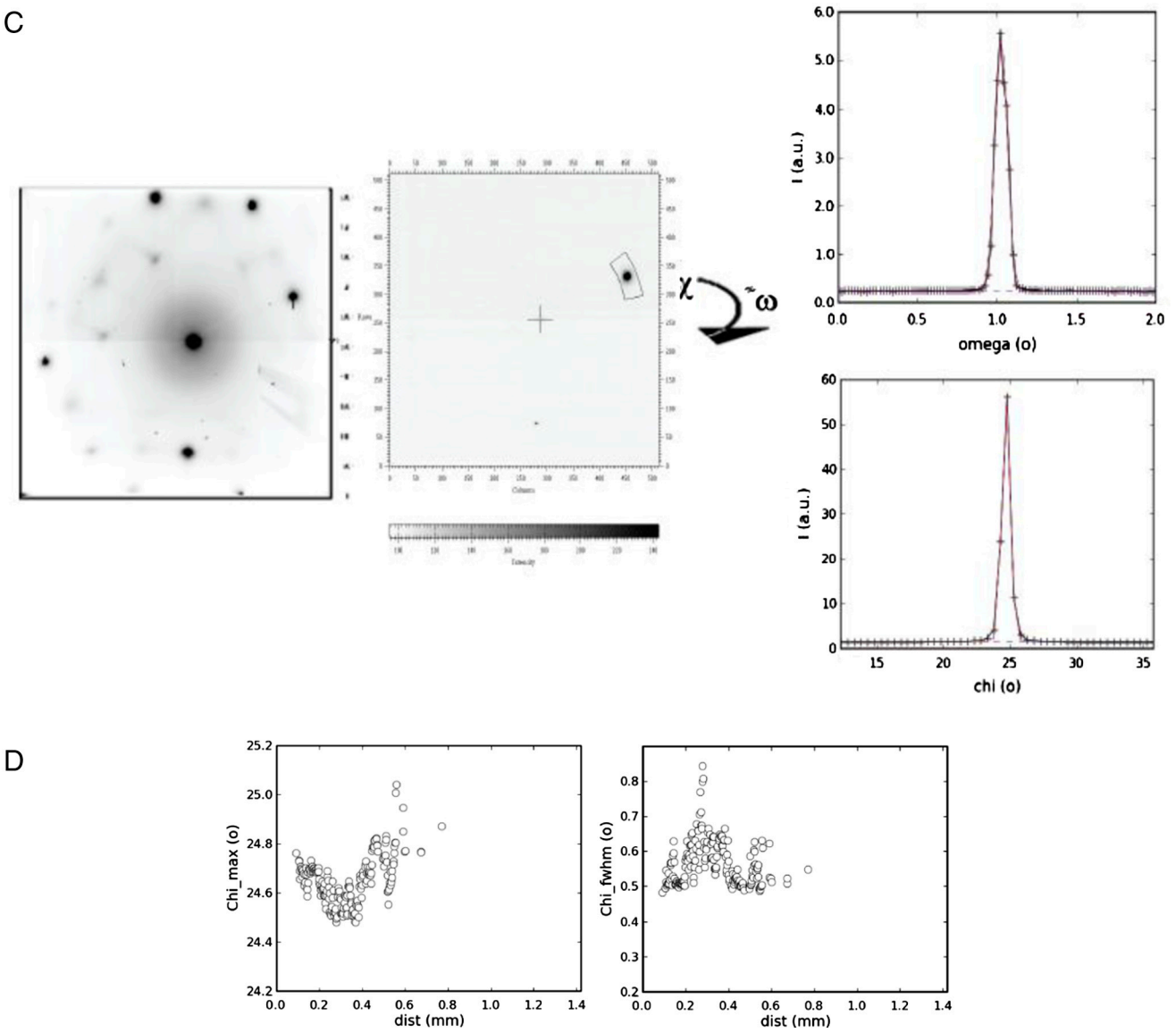

Fig. S9. (*A*) *Upper left* is the azimuthally integrated intensity *I* vs *q* where $q = 4\pi \sin(\theta)/\lambda$ is the length of the scattering vector, 2θ being the scattering angle and λ the wavelength of the radiation. *Upper right* is the same display in logarithmic units showing the −4 slope at large angles in agreement with a dense 2-phase system (S9). *Bottom left*, Porod plot Iq^4 vs q^4 used to calculate *P* and *Bottom right*, the Kratky plot Iq^2 vs *q* used to calculate *J*. The vertical lines shown in the *Bottom left* and *Upper right* plots respectively show the limits chosen for the calculations of *P* and the logarithmic slope. (*B*) Optical micrograph of the transverse sea-urchin spicule thin section in transmission light and measurement scheme: the X-ray nanobeam was normal to the section and the sample was rotated about the vertical axis within restricted angular range of ω. [scale bar = 100 μm] (*C*) sum of the diffraction patterns within $\omega = \pm 5°$ with 0.1° steps showing a part of the full single crystal diffraction signal; position of one of the peaks at maximum intensity defined by the rocking curve; azimuthal profile of the reflection (*D*) max position of the peak monitored in (*B*) over the length of the radial profile; FWHM of the peak

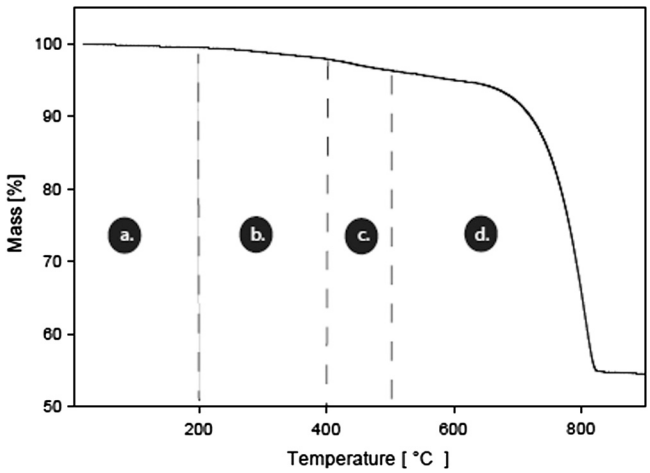

Fig. S10 Thermogravimetric analysis on cleaned, powdered sea spines. This demonstrates the temperature regimes where (*A*) loosely bound and (*B*) structural water leaves the bulk material as well as when (*C*) ACC transforms to crystalline calcite. (*D*) In the temperature range >500 °C, calcium oxide formation and chemical and structural decomposition of the sample bulk beings to occur.

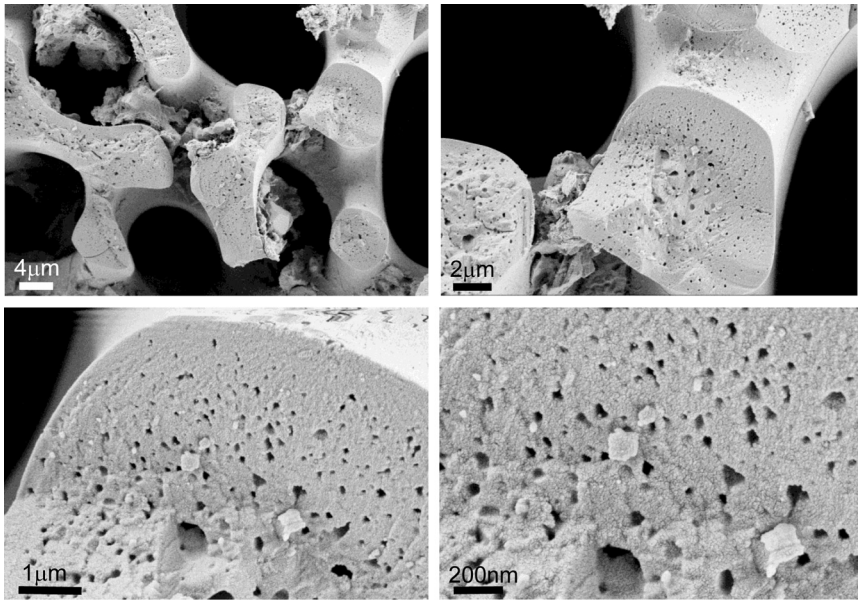

Fig. S11 SEM zoom image series for the fracture surface of a previously annealed sea urchin spine for 4 h at 450 °C.

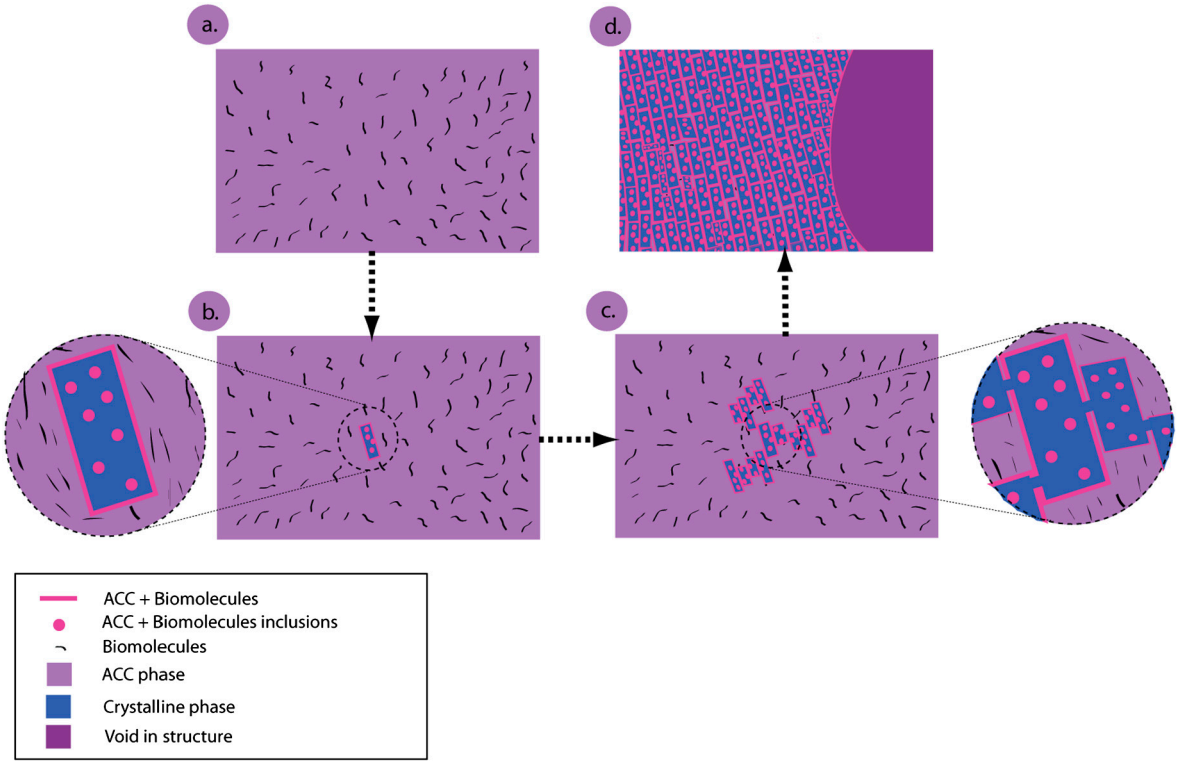

Fig. S12 Schematic model of spine formation occurring in the adult sea urchin spine (*A*). From a heterogenous state of aggregated ACC nanoparticles (not drawn for the sake of clarity) and occluded biomolecules (*B*), a single, random nucleation event occurs leading to a Mg-calcite nanoparticle with occluded ACC domains in the regions where polymers could not be further expelled via the crystal growth front. The crystal growth front pushes an ACC layer ahead which becomes increasingly rich in occluded macromolecules. Further crystallization is inhibited in analogy to impurities in the zone melting process. (Please note the color scheme—the pink regions are ACC with such high level of occluded macromolecules that crystallization is inhibited.) (*C*). However, inhomogeneities in the surface layer might still allow for further local crystallization in the form of mineral bridges through the polymer rich ACC layer. After penetrating this layer, further crystallization of a second nanocrystal can take place and proceed as for the first nanoparticle. Repetition of this process leads to a random network of nanocrystallites in an ACC matrix, which are covered by an ACC layer and are connected via mineral bridges ensuring crystalline continuity (*D*). The process continues until all ACC nanoparticles have crystallized using this mechanism.

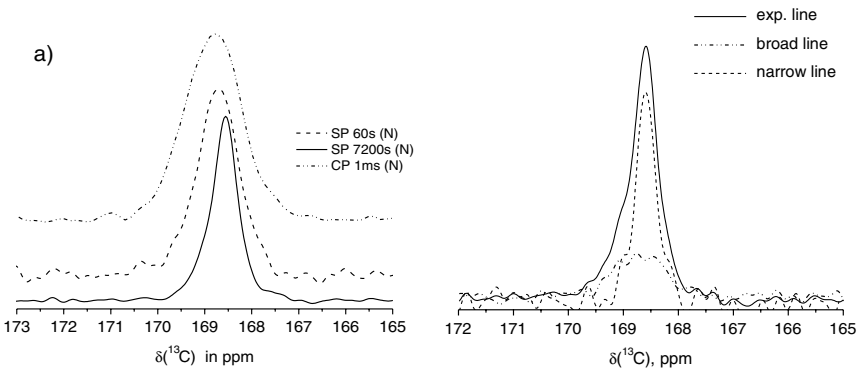

Fig. S13. (*A*) Comparison of two single pulse (SP) ^{13}C NMR spectra with repetition times of 1 min (dashed line) and 120 min (solid line) to show the presence of two differently relaxing line components and of a 1 ms CP spectrum (dash-dot). All spectra are normalized to show line shape variations. (*B*) Relaxation time editing of the experimental ^{13}C line shape: a narrow line at 168.55 ppm typical for pure calcite, and a broader component slightly shifted to 168.74 ppm appear.

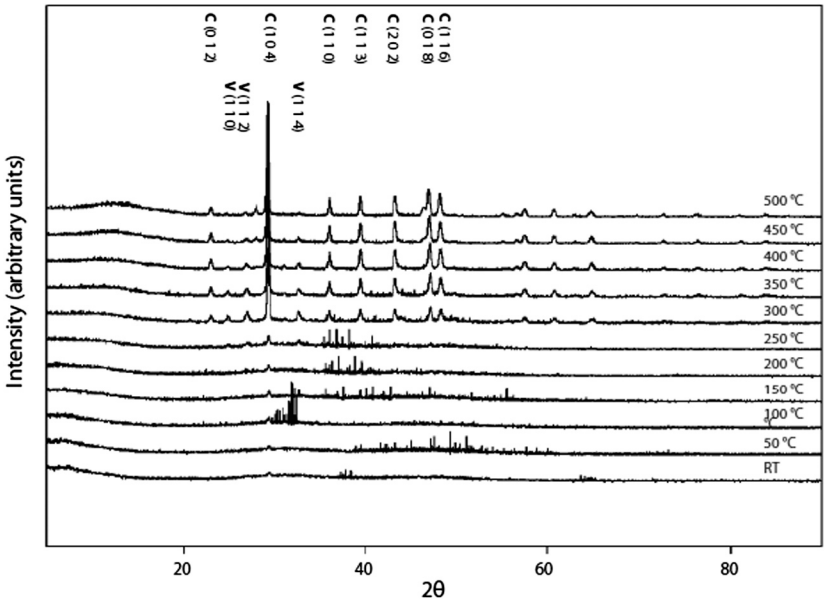

Fig. S14. Powder XRD diffractogram of synthetic ACC nanoparticles at various temperatures. Of particular interest is the (104) peak width broadening with increasing temperatures—when using the Debye-Scherrer to quantify the broadening effects, it confirms an increase in polycrystallinity in the sample with increasing temperatures.

Table S1. Crystal data, details of intensity measurements, and structure refinement

Empirical formula	$Ca_{0.96}$ $Mg_{0.04}$ C O_3
formula weight	99.46
crystal system	trigonal
space group (number)	*R*-3*c* (#167)
cell dimensions	
a, Å	4.9721(10)
b, Å	4.9721(10)
c, Å	16.952(4)
α, deg	90
β, deg	90
γ, deg	120
V, $Å^3$	362.94(14)
T, K	298
Z	6
d_{calcd}, $g{\cdot}cm^{-3}$	2.73
μ, cm^{-1}	0.2238
radiation (λ, Å)	MoKα (0.71073)
2Θ range, deg	10.62–57.94
crystal size, mm	$0.4 \times 0.3 \times 0.3$
no. of reflns measd	841
no. of unique reflns	98 ($R_{int} = 0.0353$)
no. of variable parameters	14
R (for $I > 2\sigma(I)$)	0.0142
R (for all reflections)	0.0145
wR (for all reflections)	0.0332
goodness of fit, *S*	1.142